INTERNATIONAL JOURNAL OF CLIMATOLOGY
Int. J. Climatol. (2011)
Published online in Wiley Online Library
(wileyonlinelibrary.com) DOI: 10.1002/joc.2293

RMetS
Royal Meteorological Society

Spatiotemporal structures of the intraseasonal oscillations of precipitation over northern Eurasia during summer

Yoshiki Fukutomi,[a]* Kooiti Masuda[a] and Tetsuzo Yasunari[a,b]
[a] *Research Institute for Global Change, JAMSTEC, Yokohama, Japan*
[b] *Hydrospheric Atmsopheric Research Center, Nagoya University, Nagoya, Japan*

ABSTRACT: This study identifies intraseasonal oscillations in summer precipitation over northern Eurasia using multi-channel singular spectrum analysis (MSSA) and a gridded daily precipitation data set for northern Eurasia. The analysis period is June–August of 1979–2002. Empirical orthogonal function analysis was first performed on 8-day low-pass-filtered precipitation anomalies at 2.5° grid resolution for northern Eurasia; MSSA was then carried out on the ten leading principal components (PCs). Three quasi-periodic oscillations with timescales of 45, 15, and 9 days were identified. The spatiotemporal structures of precipitation oscillations were defined by composite analysis based on the reconstructed time series of the spatiotemporal PCs obtained from the MSSA. The composite life cycle of each mode was classified into eight phase categories. The 45-day oscillation is characterised by a slow eastward progression of a broad east/west contrastive pattern which is associated with a replacement of elongated dry and wet zones across northern Eurasia. The 15-day oscillation shows a regular eastward phase propagation of precipitation anomalies with a tripole structure across the domain. The eastward displacement of dry and wet zones occurs in association with this oscillation. Spatiotemporal behaviours of the precipitation anomalies associated with the 9-day oscillation are similar to those of the 15-day oscillation, but the spatial scale of this oscillation is somewhat smaller. To explore the connections between the oscillations of precipitation and large-scale atmospheric circulation patterns, a similar composite method was applied to 300-hPa geopotential height anomalies over the Northern Hemisphere. The circulation patterns responsible for the 45-day oscillation are characterised by a wave train extending across the northeastern Atlantic/northern Eurasian sector. The wave train, with zonal wavenumbers of 3–4, indicates slow eastward moving and quasi-stationary features. The circulation patterns linked to the 15-day oscillation exhibit an eastward propagating wave train extending from northeastern Europe into the North Pacific/North American sector. In spatial scale, this wave train has zonal wavenumbers of 5–6. The wave trains associated with the 9- and 15-day oscillations have similar behaviour patterns over northern Eurasian. However, the 9-day wave train has a comparatively smaller spatial scale with zonal wavenumbers of 6–7. Therefore, the intraseasonal oscillations of precipitation are connected to the well-organised wave trains that extend from the Euro-Atlantic region to northern Eurasia, suggesting that the oscillation on each intraseasonal time scale must be produced by propagation of the corresponding wave train. Copyright © 2011 Royal Meteorological Society

KEY WORDS northern Eurasia; precipitaion; intraseasonal oscillation; multi-singular spectrum analysis

Received 10 February 2010; Revised 30 November 2010; Accepted 2 December 2010

1. Introduction

Hydrological processes in northern Eurasia play important roles in controlling changes in Arctic climate and hydrological cycles (Peng and Mysak, 1993; Wang and Cho, 1997; Peterson *et al*., 2002; Serreze *et al*., 2003; McClelland *et al*., 2004; Pavelsky and Smith, 2006; Rawlins *et al*., 2006; MacDonald *et al*., 2007; Adam and Lettenmaier, 2008). In particular, summer precipitation accounts for 30–40% of the annual total precipitation in the three major Siberian river basins (Fukutomi *et al*., 2003). The interannual variability of northern Eurasian summer precipitation also significantly affects that of the annual total precipitation and the resulting river discharge into the Arctic Ocean (Semiletov *et al*., 2000; Fukutomi *et al*., 2003). Our previous studies revealed important characteristics in the interannual variability of summer precipitation over northern Eurasia (Fukutomi *et al*., 2003, 2004, 2007). Precipitation variability was detected on time scales of about 6–8 years in eastern and western Siberia, and the spatial precipitation anomalies associated with this variability exhibited an east-west dipole pattern across northern Eurasia. Over recent decades, good progress has been made in understanding the long-term changes and variations of precipitation in northern Eurasia. The spatiotemporal characteristics of interannual variability of precipitation are understood well, along with the associated hydroclimates. However, fewer attempts have been made to investigate the intraseasonal variability of precipitation in this region.

* Correspondence to: Yoshiki Fukutomi, Research Institute for Global Change, Yokohama Institute for Earth Sciences, Japan Agency for Marine-Earth Science and Technology (JAMSTEC), 3173-25 Showa-machi, Kanazawa-ku, Yokohama, Kanagawa 236-0001, Japan.
E-mail: fukutomi@jamstec.go.jp

Intraseasonal atmospheric circulation and precipitation can be important factors in determining the seasonal characteristics of precipitation in northern Eurasia. Several recent studies have investigated the role of intraseasonal systems on summer precipitation in the lower latitudes of northern Eurasia. For instance, Iwasaki and Nii (2006) examined the Mongolian rainy season and found a break period that generally persisted for 10–20 days in July. They concluded that mid-latitude Rossby wave propagation on intraseasonal time scales caused this break period. Iwao and Takahashi (2008) discussed the roles of intraseasonal waves across northern Eurasia in producing extreme phases in a north–south seesaw pattern of summer precipitation over Northeast Asia. However, limited efforts have been made to identify the spatiotemporal structures of intraseasonal variability in the broad northern Eurasian region, including all of Siberia. As shown by Serreze and Etringer (2003), daily precipitation variability is highest during summer in the major Siberian basins. Summer is also well-known to be the most active season for the hydrological cycle in Siberia. Therefore, it is reasonable to focus on intraseasonal variability of precipitation and associated circulation in the broad northern Eurasian region during summer. One of the next steps towards understanding northern Eurasian hydroclimate is thus to explore the spatiotemporal characteristics of intraseasonal variability of precipitation.

This study examines the fundamental structures of intraseasonal oscillations of precipitation at different spatial and temporal scales in summer in northern Eurasia. A number of previous studies have attempted to detect intraseasonal oscillations of precipitation in various continental regions. By using multi-singular spectrum analysis (MSSA: Plaut and Vautard, 1994), several studies (Wang *et al*., 1996b; Ye and Cho, 2001; Krishnamurthy and Shukla, 2007) successfully identified and categorised spatiotemporal structures of the intraseasonal oscillations of precipitation in China, North America, and India. However, these structures were not detailed for northern Eurasia. Consequently, the purpose of this study is to identify spatiotemporal structures of intraseasonal oscillations of precipitation and the associated atmospheric circulation patterns over northern Eurasia during summer. To do so, we analyse a new precipitation data set of gridded daily precipitation. We first detect oscillatory modes by MSSA of daily precipitation anomalies over northern Eurasia. Then we explore the spatiotemporal structures of the isolated oscillatory modes by performing composite analysis on the precipitation fields based on the MSSA results. To reveal the evolution of large-scale atmospheric circulation patterns linked to each oscillatory mode, we also examine composites of geopotential height anomalies over the Northern Hemisphere. This article is organised as follows: Section 2 briefly describes the data and data-processing methods used. Section 3 presents the climatological features of the summer precipitation. Section 4 explains the MSSA procedure employed and presents characteristics of the oscillatory modes identified by MSSA. Section 5 describes the spatiotemporal structures of the oscillations. Section 6 examines the large-scale circulation patterns associated with the oscillations. Finally, Section 7 presents a summary and discussion.

2. Data sources and processing

To determine primary modes of intraseasonal precipitation variability over northern Eurasia, we used gridded daily precipitation data obtained from the Research Institute for Humanity and Nature (RIHN) in Japan (http://www.chikyu.ac.jp/precip/index.html). This precipitation data set was developed as part of the Asian Precipitation–Highly Resolved Observational Data Integration Towards the Evaluation (APHRODITE) of the water resources project (Yatagai *et al*., 2008, 2009; Takashima *et al*., 2009). The precipitation data set covers a broad portion of continental Eurasia including East Asia, Southeast Asia, South Asia, North Asia, the Middle East, and northern Eurasia. We used the northern Eurasian subset which is available for the period 1979–2002. The original subset contains daily gridded precipitation with a horizontal resolution of 0.5°. We re-gridded the original precipitation fields into 2.5° by a simple area averaging method.

We also used an atmospheric reanalysis data set to explore large-scale atmospheric circulation patterns associated with precipitation oscillatory modes. The reanalysis data set, the Japanese 25-year reanalysis (JRA25), was recently produced by the Japan Meteorological Agency (JMA) Numerical Assimilation and Forecast System and provides many assimilated and forecasted variables available at a 6-h temporal resolution and various grid types (Onogi *et al*., 2005, 2007). We used the 300-hPa geopotential height and zonal and meridional winds on horizontal 2.5° grids from the "anl_p25" subset of JRA25 (Onogi *et al*., 2007). The data were daily-averaged before analysis.

The data analysis was carried out for a 24-year period from 1979 to 2002 when both the northern Eurasian precipitation analysis and JRA25 were commonly available. The anomaly time series of all variables were computed by subtracting the first three harmonics from the original 365-day time series to remove the seasonal cycle. The precipitation anomaly time series were then filtered to extract intraseasonal components by using the low-pass filter of Kaylor (1977), which removes periods of <8 days corresponding to synoptic time scale fluctuations.

3. Climatological features

3.1. Summer mean precipitation

We first present summer precipitation climatology in northern Eurasia. The mean precipitation for June–August (JJA) 1979–2002 is shown in Figure 1. The features in this climatology are basically similar to those demonstrated by Fukutomi *et al*. (2003, 2004). The summer Siberian precipitation zone is evidently seen.

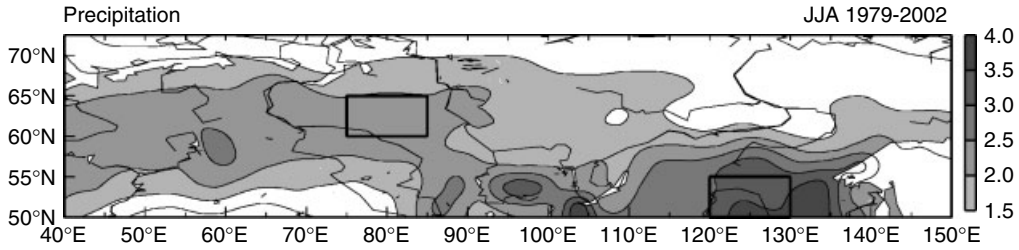

Figure 1. Twenty-four-year (1979–2002) climatology of the June–August (JJA) mean precipitation over northern Eurasia. Contour interval is 0.5 mm day^{-1}. Regions with values >1.5 mm day^{-1} are shaded. The eastern and western Siberian domains for the spectral analysis are indicated by black boxes.

A prominent band of precipitation exceeding 2 mm day^{-1} extends from the east of Lake Baikal to the Far East Asian coast along 50°N to 60°N. In particular, local precipitation maxima >3 mm day^{-1} are concentrated in this band. These enhanced precipitation signals might reflect effects of the mountain orography in the southern part of central-eastern Siberia. Another band of enhanced precipitation extends from European Russia to western Siberia along 55°N to 65°N. The Siberian precipitation zone corresponds closely to the area of maximum extratropical cyclone and frontal activity over northern Eurasia (Serreze *et al*., 2001; Serreze and Etringer, 2003; Yoon and Chen, 2006; Fukutomi *et al*., 2007). These previous studies discussed the maintenance of the Siberian precipitation zone.

3.2. Spectral properties

Prior to performing MSSA, we computed power spectra for precipitation for JJA 1979–2002 to briefly detect dominant intraseasonal time scales in northern Eurasia. A fast Fourier transform (FFT) technique was employed for calculating these spectra based on the procedure of Fukutomi and Yasunari (2005). The power spectra for each JJA period were averaged over 24 years to obtain ensemble averaged spectra. Precipitation indices for the spectral computation were defined as precipitation time series averaged over the two domains where the mean precipitation was comparatively larger in the Siberian region (Figure 1). One was the eastern Siberian domain bounded by 50°N to 55°N, 120 °E to 130 °E, and another was the western Siberian domain enclosed by 60°N to 65°N, 75 °E to 85 °E. The resulting power spectra are given in Figure 2. The spectrum for the eastern Siberian precipitation index (Figure 2(a)) shows two peaks significant at the 95% confidence level within the typical submonthly (6–30 days) range. A maximum peak and a secondary maximum peak are observed at 11 and 9 days, respectively. However, pronounced spectra are found in both the lower-frequency intraseasonal (>30 days) and submonthly range for the western Siberian precipitation index (Figure 2(b)). The spectra at 43 and 16 days are actually significant at the 95% confidence level. These spectra suggest that the submonthly variability is prominent in broad Siberia and the low-frequency intraseasonal variability is dominant in western Siberia. These features

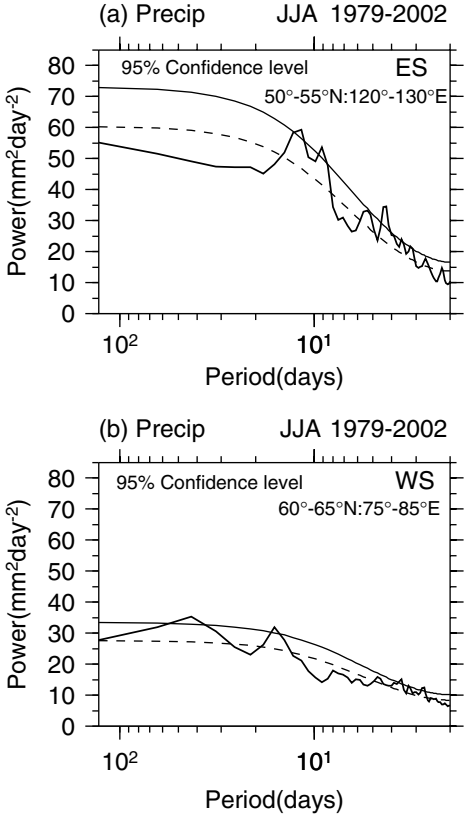

Figure 2. (a) Twenty-four-summer (JJA 1979–2002) ensemble power spectrum of precipitation averaged over the eastern Siberian domain (50°N to 55°N, 120 °E to 130 °E). The thin solid curve is the 95% confidence level. Dashed curve is the red noise spectrum. (b) Same as (a) except for the western Siberian domain (60°N to 65°N, 75 °E to 85 °E).

are confirmed by the MSSA results presented in later sections.

4. Application of MSSA to the precipitation anomalies

4.1. Overview

We applied multi-channel singular spectrum analysis (MSSA) to the precipitation data to identify modes of intraseasonal variability of precipitation over northern Eurasia. Many studies have reported MSSA to be an effective tool for isolating quasi-periodical oscillating modes of atmospheric and oceanic variability on

intraseasonal to interannual time scales (Plaut and Vautard, 1994; Dettinger *et al*., 1995; Jiang *et al*., 1995; Wang *et al*., 1996a, 1996b; Moron, 1997; Wang and Cho, 1997; Zhang *et al*., 1997, 1998; Moron *et al*., 1998; Qian *et al*., 2000; Simonnet and Plaut, 2001; Ye and Cho, 2001; Krishnamurthy and Shukla, 2007, 2008). A detailed description of MSSA procedure was first provided by Plaut and Vautard (1994). They performed MSSA on 700-hPa geopotential heights to identify recurrent intraseasonal circulation patterns in the wintertime Northern Hemisphere extratropics. Subsequently, several studies successfully detected regional oscillations of precipitation using MSSA (Wang *et al*., 1996b; Wang and Cho, 1997; Qian *et al*., 2000; Ye and Cho, 2001; Krishnamurthy and Shukla, 2007). Other studies have applied MSSA to sea level pressure, surface air temperature, and sea surface temperature (Dettinger *et al*., 1995; Jiang *et al*., 1995; Moron, 1997; Moron *et al*., 1998; Zhang *et al*., 1998; Simonnet and Plaut, 2001). Thus, MSSA has been widely used to capture space–time patterns of climatic oscillations in various fields. As explained by the above papers, MSSA is an extension of empirical orthogonal function (EOF) analysis and equivalent to an extended EOF analysis. Basically, MSSA consists of two steps. The first is a conventional EOF analysis of a particular data field (time series at grid points) to obtain its principal components (PCs). The second is to solve an eigenvalue problem of a lag cross-covariance matrix constructed from the leading PCs which are viewed as multi-channel series. Generally, eigenvectors and PCs resulting from the second step are referred to as space–time EOFs (ST-EOFs) and space–time PCs (ST-PCs), respectively (Plaut and Vautard, 1994). These elements consolidate information on both the spatial and temporal variability of eigenmodes derived from MSSA.

In this study, MSSA was applied to daily precipitation anomalies in northern Eurasia basically following the procedure of Wang *et al*. (1996a) and Krishnamurthy and Shukla (2007, 2008). In particular, we referred to Krishnamurthy and Shukla (2007, 2008) for carrying out MSSA using a multi-year set of daily data for a particular season. To investigate space–time structures of intraseasonal oscillations of precipitation, we analysed the 92-day period from 1 June to 31 August (JJA) of each year from 1979 to 2002. We prepared a 24-year set of precipitation data from mid-April to mid-October to incorporate a lag window length for MSSA. In the following sections, we briefly describe the MSSA procedure and initial results. We do not present the mathematical formulation of MSSA because that has been given in previous works (Plaut and Vautard, 1994; Jiang *et al*., 1995; Wang *et al*., 1996a; Wang and Cho, 1997; Qian *et al*., 2000), which can also be referred to for general technical details of MSSA.

4.2. Spatial EOF analysis

An EOF analysis was performed on the 8-day low-pass-filtered precipitation anomalies from 17 April to 15 October (182 days) from 1979 to 2002 (24 years) in northern Eurasia (50°N to 70°N, 40°E to 140°E). The total data length (182 days) for each year was the targeted analysis period and a length associated with a lag window for MSSA. The targeted analysis period was the 92 days from 1 June to 31 August (JJA). The remaining 90 ($182 - 92$) days was the period associated with the lag window length (M) defined by the subsequent MSSA. Since we used a lag window length of 91 days ($M = 91$), we had to add a 90-day-long ($M - 1 = 90$) time series to the time series of the targeted analysis period. This 90-day period was divided into two 45-day periods, pre- and post-JJA: 17 April to 31 May and 1 September to 15 October, respectively. Note that the total length of the time series to be analysed by the EOF analysis was $182 \times 24 = 4368$ days.

As a result of the EOF analysis, we obtained spatial principal component (S-PC) time series and corresponding spatial EOF (S-EOF) patterns. We used the leading ten S-PCs, which account for about 53% of the total variance, as ten channels for the subsequent MSSA. The leading ten S-EOF patterns are shown in Figure 3. Most of the S-EOFs exhibit east-west or wave-like patterns and several other modes show zonally elongated band structures spanning most of the area studied. S-EOF 1 indicates the highest fluctuations in the southeastern part of the study area; S-EOFs 2 and 3 represent northwest–southeast oriented wave-like patterns; S-EOFs 4, 5, and 7 show zonally elongated band structures and S-EOF 6 is characterised by the largest anomalies in the southern part of central Siberia. S-EOFs 8, 9, and 10 show comparatively smaller-scale wave-like patterns. Therefore, it would appear that the S-EOFs of the precipitation anomalies in the northern Eurasian domain have well-organised structures.

4.3. Oscillatory modes identified by MSSA

The first ten S-PCs directly formed a multi-channel series with ten channels ($L = 10$; L is the number of channels) for MSSA. We computed a cross-covariance of the multi-channel series at 91 lags ($M = 91$) and then produced a lag cross-covariance matrix for the entire period (17 April to 15 October of 1979–2002) with $(L \times M) \times (L \times M)$ dimensions. The main process of the MSSA was to solve an eigenvalue problem for this matrix. By doing this, we finally derived space–time eigenvectors and corresponding space–time PCs (ST-PCs). The ST-PC is a time series of 92-day length for each year which represents the temporal evolution of space–time eigenmodes. The space–time eigenvector is referred to as ST-EOF and is 91 days in length. The ST-EOF represents a pattern of the space–time eigenmodes in the time dimension.

As a result of the MSSA, we obtained $L \times M = 910$ space–time eigenmodes composed of ST-PC k and ST-EOF k ($k = 1, 2, \ldots, 910$, where k is the order of the modes) and the corresponding eigenvalues. A quasi-periodic oscillatory mode is basically defined by a pair of successive eigenmodes in the order k and $k + 1$,

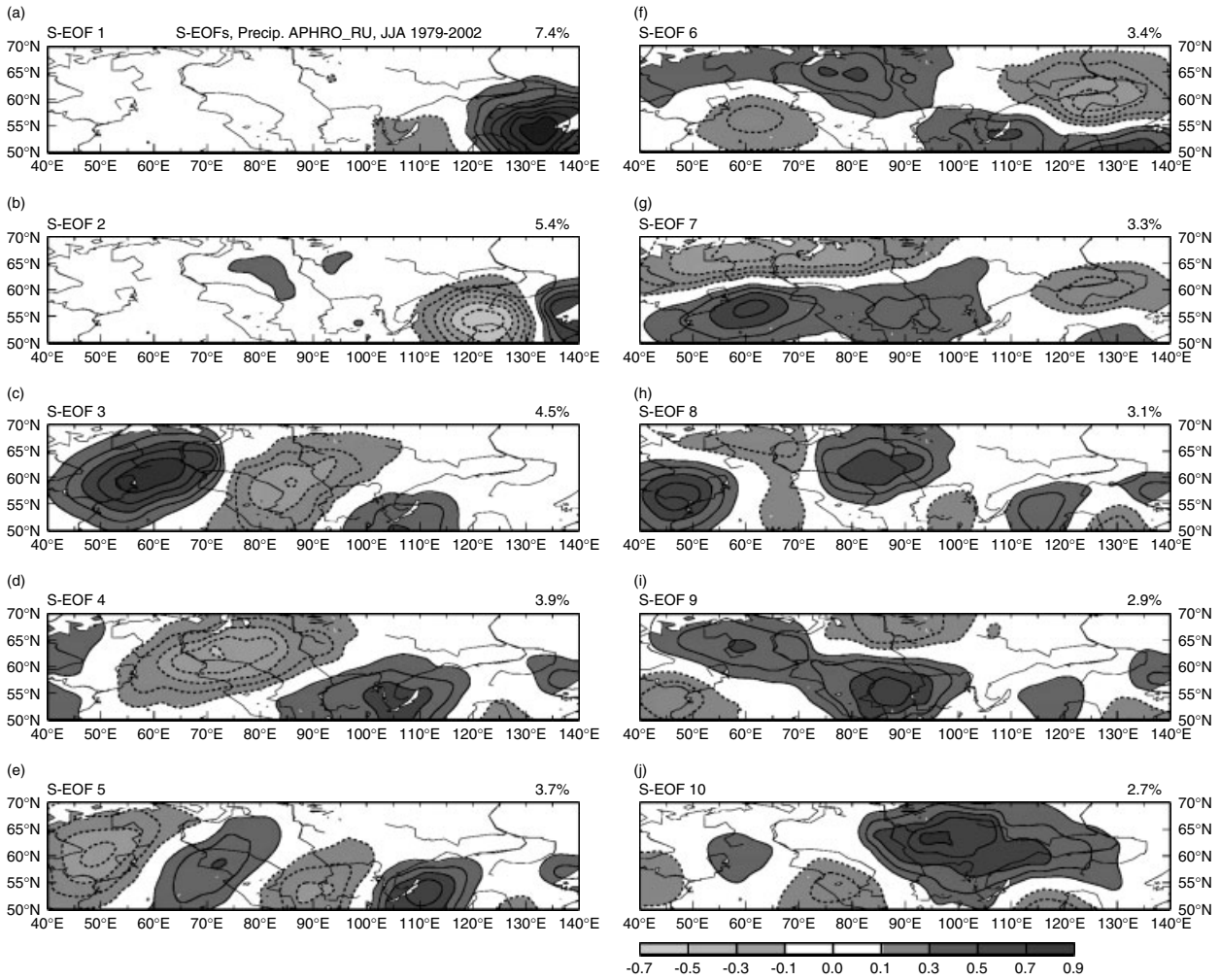

Figure 3. Spatial patterns of the first 10 S-EOFs of precipitation anomalies over northern Eurasia. Contour interval is 0.1 (unit of correlation coefficient). Positive (negative) anomalies are drawn with solid (dashed) contours. Zero contours are omitted. Positive (negative) anomalies are lightly (darkly) shaded.

which have nearly equal eigenvalues (Plaut and Vautard, 1994; Wang *et al*., 1996a). That is, ST-PCs k and $k+1$ reflect an oscillation on the same time scale and are in quadrature with each other. Here they are represented as an oscillatory pair $k-k+1$. To identify a dominant time scale of each oscillatory mode, power spectrum analysis by the maximum entropy method (MEM) was carried out on the ST-PCs following Wang *et al*. (1996a). In this analysis, ST-PCs 1 and 2, 5 and 6, and 14 and 15 had peaks in their maximum entropy (ME) power spectra at 15, 45, and 9 days, respectively (not shown). Therefore, these ST-PCs form three oscillating pairs: 1-2, 5-6, and 14-15 (hereafter denoted as ST-PCs 1-2, ST-PCs 5-6, and ST-PCs 14-15). The ME power spectra of these three pairs are shown in Figure 4, plotted in the form of a variance fraction of the sum of the spectra of the paired modes. The variance fraction was estimated as a percentage of the total variance defined by the sum of the spectra of all ST-PCs (Plaut and Vautard, 1994; Wang *et al*., 1996a). It was confirmed that the spectra of ST-PCs 1-2, ST-PCs 5-6, and ST-PCs 14-15 had peaks at 15, 45, and 9 days, respectively.

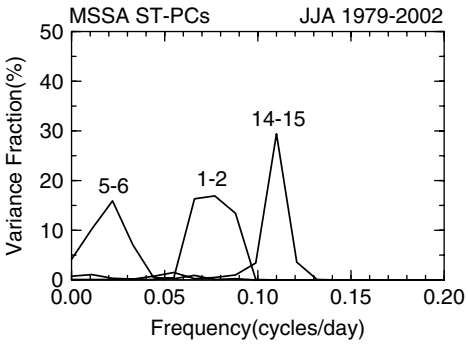

Figure 4. ME power spectra of three ST-PC pairs (ST-PCs 1-2, ST-PCs 5-6, and ST-PCs 14-15) derived by MSSA in the form of variance fraction (%).

Overall, ST-PCs 1-2 corresponded to a 15-day oscillation fluctuating within a range of 10–20 days. ST-PCs 5-6 exhibited a 45-day oscillation which included fluctuations on time scales longer than about 30 days. ST-PCs 14-15 gave a 9-day oscillation, substantially a quasi-10-day oscillation. Characteristics of the three oscillating pairs are summarised in Table I. Here, one can notice that

Table I. Characteristics of the oscillatory pairs $(k,\ k+1)$ identified by the MSSA.

Pair	Period (days)	Variance (%)	Peak variance (%)
1–2	15	3.8	16.4
5–6	45	3.4	15.9
14–15	9	2.6	29.5

The first column gives the order number of the pair. The second column contains the period of oscillation at the peak value of the ME spectra of each pair (Figure 4). The third column shows the total percentage variance explained by each pair which is estimated from the eigenvalues of the MSSA results. The fourth column gives the percentage variance at the peak frequency of the ME spectra of each pair (Figure 4).

these time scales identified by MSSA are similar to those detected by the FFT-based spectrum analysis in the previous section. It should also be noted that these three oscillations were reproducible by MSSA with other lag window sizes. We also examined $M = 61$ and $M = 51$ cases, and the resulting spectral characteristics were similar to those for the present $(M = 91)$ case. This implies certain robustness in these oscillations.

A space–time reconstructed component (RC) of each MSSA eigenmode was computed for the 182-day period of each year following the mathematical formula of Plaut and Vautard (1994). In their formula, the RC for each channel is constructed from the corresponding ST-PC and ST-EOF. The resulting RC is a time series which represents the time evolution of each channel series on the time scale of the corresponding MSSA eigenmode. In other words, the RC is equivalent to a filtered component of the original S-PC.

The time series of paired RCs of an oscillation is the sum of the RCs of the oscillatory pair $(k,\ k+1)$ (Plaut and Vautard, 1994; Wang *et al.*, 1996a; Krishnamurthy and Shukla, 2007, 2008). The time series of the paired RCs of the 15-, 45-, and 9-day oscillations are denoted as RCs 1-2, RCs 5-6, and RCs 14-15, respectively. Example time series of the paired RCs are displayed in Figure 5. In each panel, the quasi-periodical oscillating nature of each mode is obvious. Channel 1 was chosen to plot RCs 1-2 and RCs 14-15 (the 15- and 9-day oscillations) and channel 3 was chosen for RCs 5-6 (the 45-day oscillation). The RC for the chosen channel has maximal variance among all the RCs for ten channels of each MSSA eigenmode. Also, the time series of the paired RCs for the chosen channel was used as an index for composite analysis, described in the next section.

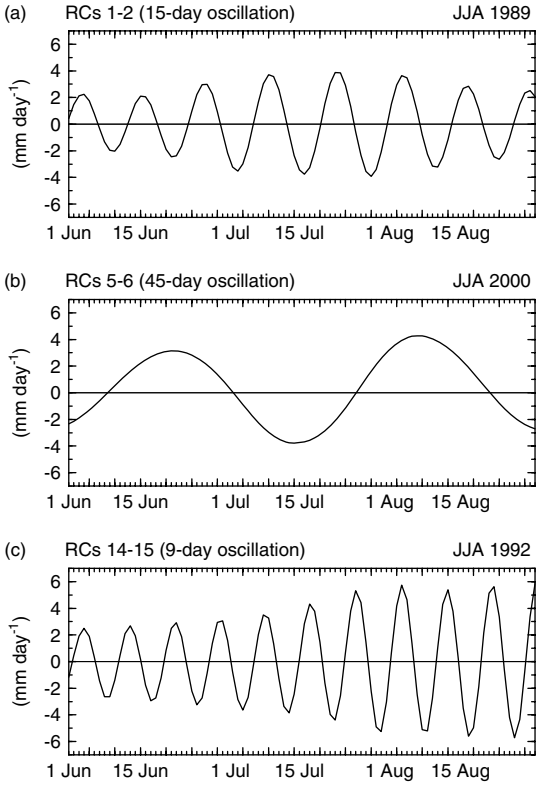

Figure 5. Time series of RCs corresponding to ST-PCs. (a) RCs 1-2 (15-day oscillation) in channel 1 for JJA 1989. (b) RCs 5-6 (45-day oscillation) in channel 3 for JJA 2000. (c) RCs 14-15 (9-day oscillation) in channel 1 for JJA 1992.

5. Space–time structures of the oscillations of precipitation

5.1. Composite analysis

Three distinct oscillations of precipitation were identified by the MSSA. We conducted composite analysis to examine the space–time evolution of these oscillations, using the time series of paired RCs as an index to construct composites. The phase compositing technique based on the RC has been described in detail in several papers (Plaut and Vautard, 1994; Wang *et al.*, 1996a; Krishnamurthy and Shukla, 2007, 2008). We basically followed the technique and determined instantaneous phases of the oscillation. A cycle of oscillation was divided into eight phase categories and the space–time composited fields were keyed to these eight phases, denoted as phase 1 to phase 8. The time intervals between consecutive phases were supposed to be almost equal. A positive (negative) peak of the oscillation was assigned as phase 3 (phase 7). The point at which an increasing (decreasing) index curve crossed zero was assigned as phase 1 (phase 5). The remaining phases 2, 4, 6, and 8 were intermediate phases. The composite structures of phases 1–4 were considered out of phase with those of phases 5–8. Cycles of oscillation for the composite analysis were chosen using the RC-based index of each mode. We employed 1.5 standard deviation of the index for the entire period as a criterion to identify the peak phases of the oscillation (phases 1 and 8). We eventually chose cycles of oscillation which included the peak phases that satisfied this criterion. Thus, space–time structures of the three distinct oscillatory modes were obtained by composite analysis of precipitation anomalies during JJA based on the index of the three oscillatory modes. Space–time fields of precipitation anomalies used for the composite analysis were

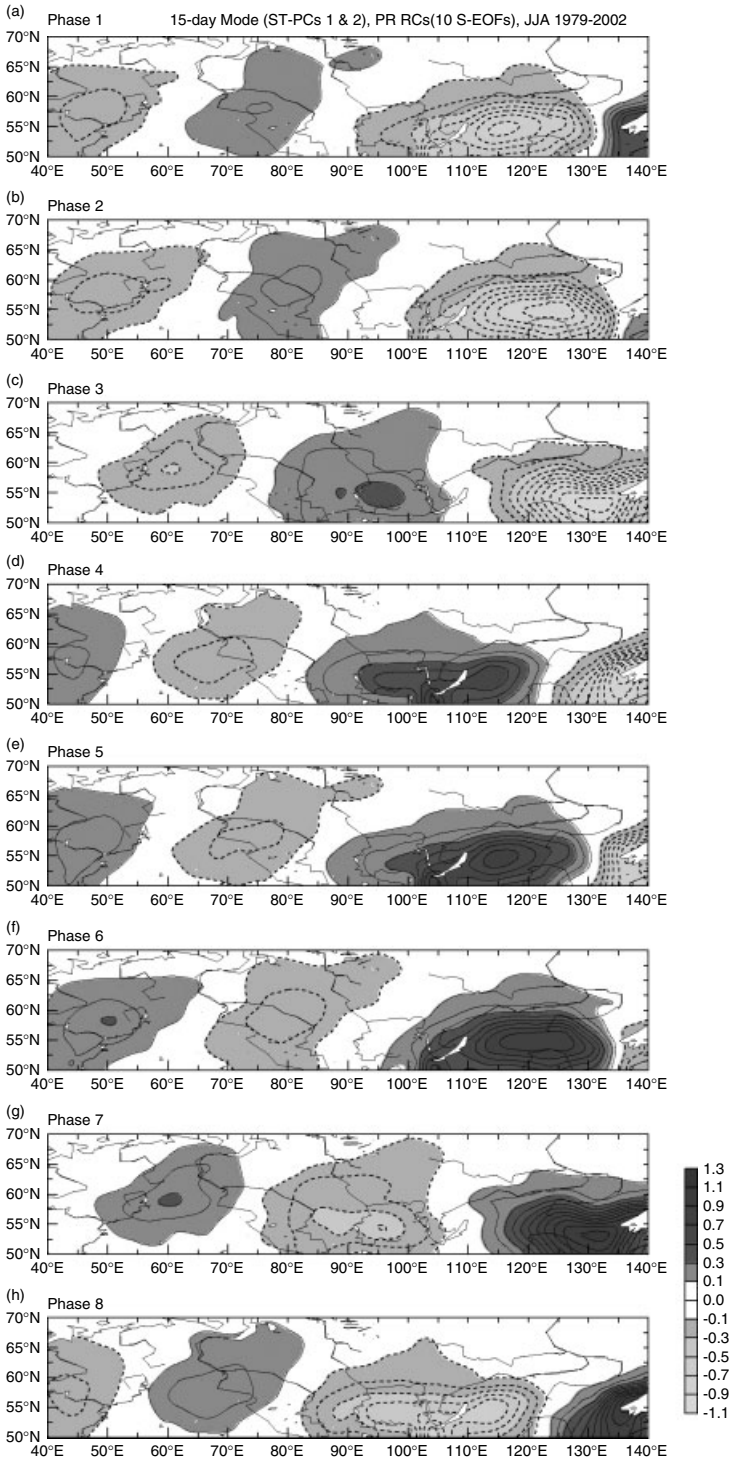

Figure 6. Spatial–temporal structures of the 15-day oscillation of precipitation over northern Eurasia, represented by composites of reconstructed precipitation anomalies (mm day^{-1}) keyed to phase categories 1–8. Contour interval is 0.1. Positive (negative) anomalies are drawn with solid (dashed) contours. Zero contours are omitted. Positive (negative) anomalies are lightly (darkly) shaded.

reconstructed by projecting the RCs for all channels of the oscillatory mode onto their respective S-EOFs. The space–time fields were reproduced separately for each oscillatory mode.

5.2. The 15-day oscillation

The 15-day mode is the strongest intraseasonal oscillation of precipitation over northern Eurasia indicated by the MSSA eigenmode pairs (ST-PCs) 1 and 2. Figure 6 displays composite space–time structures of the 15-day oscillation. A total of 57 cycles of the oscillation were used to construct the composites. Precipitation anomalies exhibit regular eastward phase propagation of a zonally oriented tripole pattern with positive (anomalous wet zone) and negative anomalies (anomalous dry zone). In phase 1, the precipitation anomalies are characterised by

an east-west dipole pattern between western and eastern Siberia. Comparatively weaker positive anomalies cover western Siberia, whereas stronger negative anomalies cover eastern Siberia. An anomalous wet zone moves eastward to central Siberia by phase 3 and then arrives at eastern Siberia by phase 5. In phase 5, an anomalous dry zone over eastern Siberia in phase 1 is completely replaced with a strong wet zone from the west. Another dry zone prevailing over European Russia in phase 1 moves towards western Siberia by phase 5. The whole pattern in phase 5 becomes almost out of phase with that in phase 1. After phase 5, the wet anomalies strengthen in the southern part of eastern Siberia. This wet zone continues travelling eastward and disappears towards the North Pacific by phase 8. Meanwhile, a new dry zone arrives over eastern Siberia. We notice that another wet zone is established in European Russia from phase 3 through phase 5. This wet zone moves to western Siberia by the next phase 1. Thus, the composite sequence of this mode shows a clear recurrent cycle. Overall, the 15-day mode produces an apparent eastward displacement of the anomalous dry and wet zones across northern Eurasia associated with the eastward phase propagation. Both the positive and negative precipitation anomalies become stronger as they move eastward in the Siberian region. In particular, the southern part of eastern Siberia corresponding to the upper Lena River basin is covered with the strongest anomalies.

5.3. The 45-day oscillation

The 45-day mode is characterised by a broad east-west contrastive pattern in the entire area of northern Eurasia. This mode is represented by ST-PCs 5 and 6. Figure 7 presents a composite evolution of the 45-day oscillation. A total of 17 cycles of the oscillation were selected for the compositing. A zonally elongated anomalous wet zone appears over European Russia in phase 2 and a zonally elongated anomalous dry zone appears over western-central Siberia at the same time. Another distinct dry zone develops on the southeastern edge of the study area. The distinct dry zone eventually combines with the zonally elongated dry zone from the west. The wet zone progresses slowly eastward into central Siberia by phase 5. At the same time, wet (positive) anomalies are dominant in western Siberia and dry (negative) anomalies dominated in eastern Siberia. After phase 6, as the western Siberian wet zone continues to extend towards eastern Siberia, a new dry zone extends eastward from European Russia into western-central Siberia. The wet zone is then replaced by the dry zone in this region between phases 6 and 8. In addition, the distinct dry zone is replaced with a new distinct wet zone by phase 6, which is then merged with the wet zone moving from the west. Compared with the 15-day mode, the 45-day mode indicates zonally elongated band structures of the dry and wet zones throughout its life cycle. The zonal extent of individual dry and wet zones is larger than that of the 15-day mode. In addition, the 45-day mode indicates stronger fluctuations in European Russia through western and central Siberia. There are characteristic east-west dipole patterns between European Russia and western and central-eastern Siberia around phases 3 and 7 in particular. The eastward progression of the dry and wet zones may reflect a replacement of an above (below) normal precipitation episode by a below (above) one in European Russia and western Siberia (central-eastern Siberia) and vice versa. Each regional precipitation episode might last for about 2 weeks. For example, the dry episode persists for at least three phases from phases 1 to 3, while the wet episode persists from phases 5 to 7 over central Siberia.

5.4. The 9-day oscillation

The 9-day mode corresponds to ST-PCs 14 and 15, which has a comparatively smaller spatial scale than the other two modes. Strong precipitation fluctuations associated with the 9-day oscillation are confined to the southeastern part of northern Eurasia. Figure 8 gives space–time structures of the 9-day oscillation. A total of 54 cycles of the oscillation were chosen to create the composite fields. Eastward and southeastward propagation of precipitation anomalies is evident across the domain, similar to the 15-day oscillation. This mode contributes less to precipitation fluctuations over European Russia and western Siberia. As the anomalies increase eastward, their amplitude becomes larger and reaches maxima in the southern part of central-eastern Siberia. In particular, both positive and negative anomalies develop over the upper Yenisey River basin/Lake Baikal area and the southern upper Lena River basin. From phase 2 to phase 3, an east-west dipole pattern with eastern positive and western negative anomalies is evident. An almost opposite pattern appears during phases 6 and 7. A localised displacement of drier and wetter zones occurs in these regions throughout the life cycle of this oscillation.

6. Large-scale circulation patterns associated with the oscillations of Precipitation

The previous section identified the space–time structures of the three oscillatory modes of intraseasonal precipitation over northern Eurasia. Our next concern is the structure and evolution of a large-scale atmospheric circulation pattern that produces each precipitation oscillatory mode. The space–time alternation of anomalous dry and wet zones over northern Eurasia presumably results from specific atmospheric circulation systems. To establish the relationships between the precipitation oscillatory modes and atmospheric circulation patterns, we applied a similar composite method to 300-hPa geopotential height anomaly fields in the Northern Hemisphere. The wave activity flux vector derived by Takaya and Nakamura (1997, 2001) was used to diagnose the propagating Rossby wave nature of the composited circulation pattern. We employed the two-dimensional formulation of the stationary wave activity flux used by Jiang and Lau

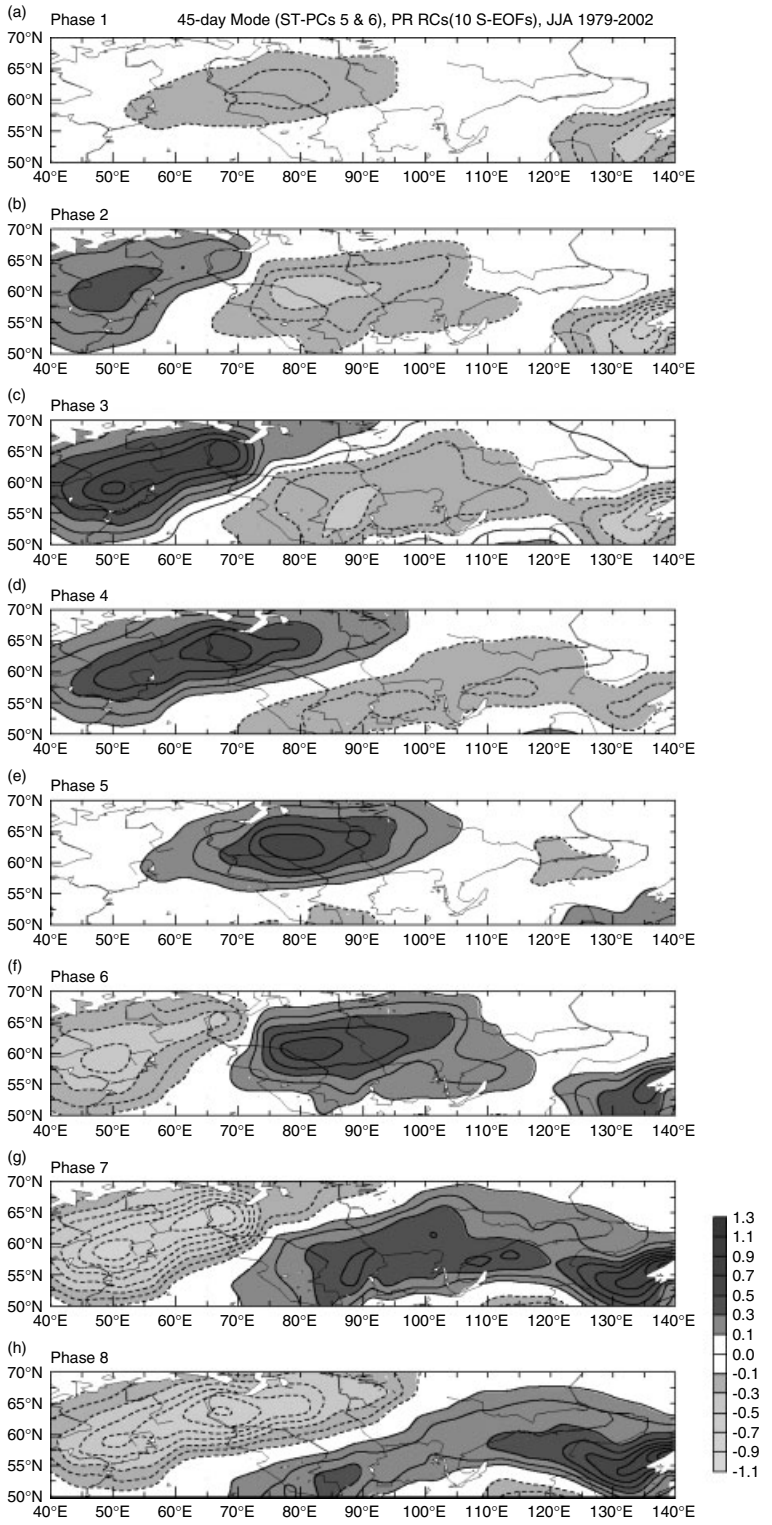

Figure 7. Same as Figure 6 except for the 45-day oscillation.

(2008). Perturbation geostrophic wind and geostrophic stream function were estimated from the composited geopotential height anomalies at 300 hPa to compute the wave activity flux. The summer (JJA) averaged zonal and meridional winds at 300 hPa were also used.

Figure 9 shows a composite evolution of 300-hPa geopotential height anomalies together with horizontal wave activity flux vectors over the mid- and high-latitude Northern Hemisphere associated with the 15-day oscillation of precipitation. The geopotential height anomalies were 8- to 25-day band-pass filtered before compositing to gain a clearer picture of the atmospheric circulation pattern, which is responsible for the submonthly scale oscillation. A circulation pattern exhibits an eastward-travelling wave train originating in northeastern Europe and extending into the North

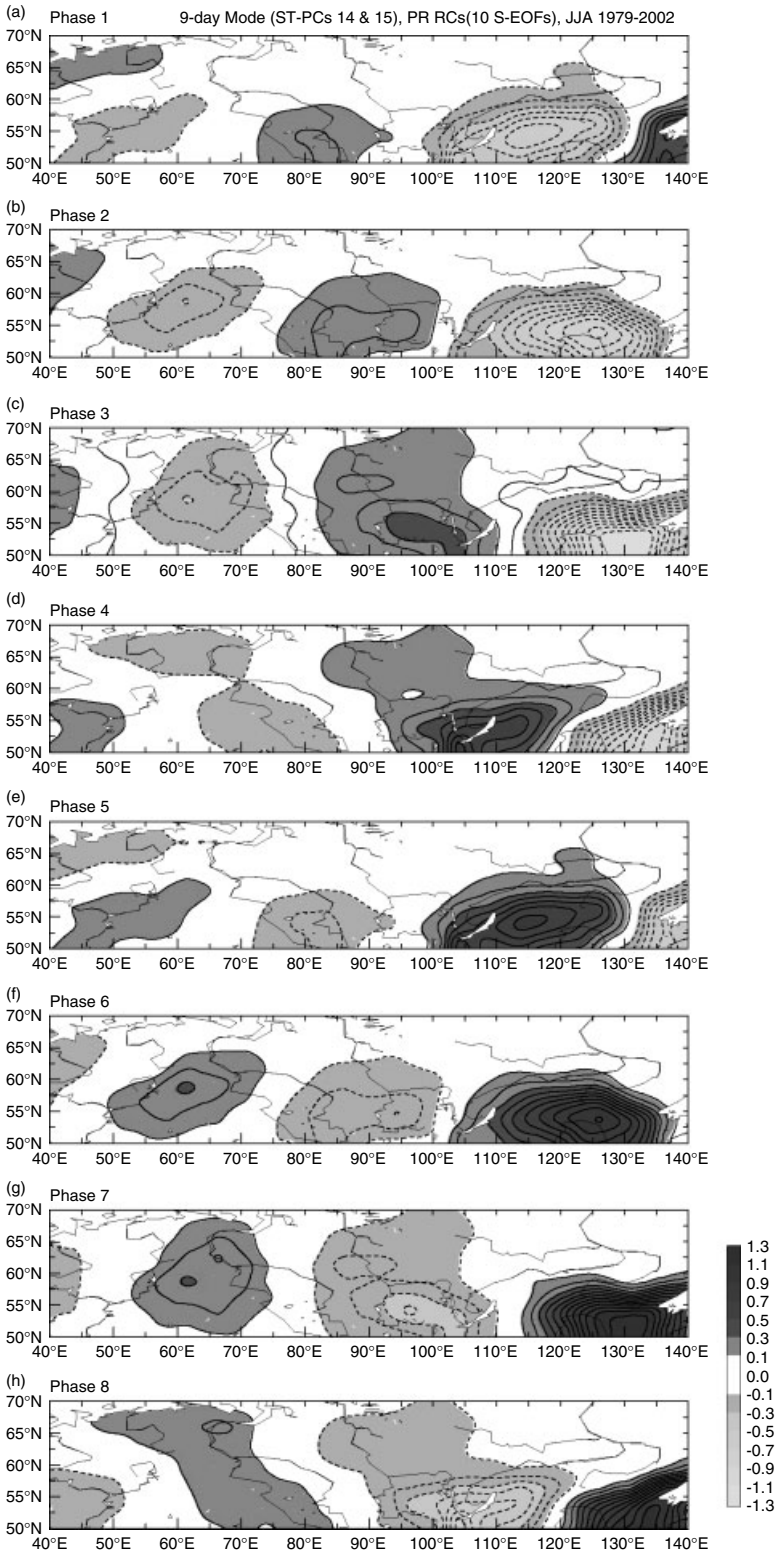

Figure 8. Same as Figure 6 except for the 9-day oscillation.

Pacific/North American sector throughout the life cycle. The wave train consists of meridionally elongated anomalous troughs and ridges with a spatial scale of zonal wavenumbers 5–6. The waves propagate eastward from northeastern Europe into central Siberia and then southeastward from central Siberia into Far East Asia and the northwestern Pacific. As the waves propagate eastward, the anomalous troughs and ridges are strengthened in the eastern part of northern Eurasia. Comparing the precipitation composite (Figure 6), we notice that locations of the eastward moving troughs (ridges) almost corresponded to those of the anomalous wet (dry) zones at each phase, suggesting that this wave train dominates the 15-day precipitation oscillatory mode. The eastward–southeastward

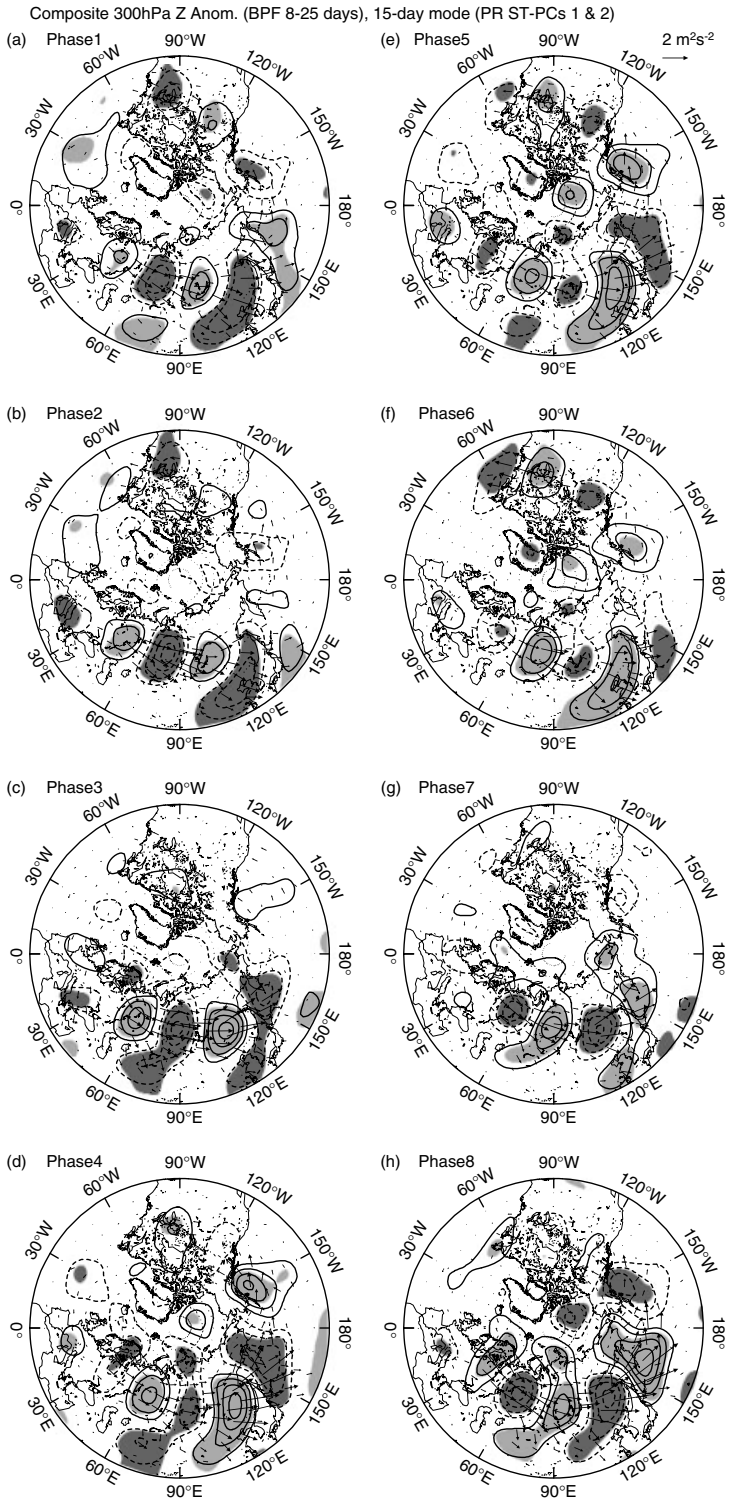

Figure 9. Composites of 300-hPa geopotential height anomalies (8- to 25-day band-pass filtered) over the Northern Hemisphere keyed to phase categories 1–8 of the 15-day oscillation and corresponding wave activity flux vectors ($m^2\ s^{-2}$). Contour interval is 10 m. Positive (negative) anomalies are drawn with solid (dashed) contours. Zero contours are omitted. Positive (negative) anomalies with statistically significant at 95% level are lightly (darkly) shaded.

phase propagation and downstream amplification features of the northern Eurasian wave packet are consistent with those of the precipitation anomalies of the 15-day mode (Figure 6). The downstream amplification of the waves could have been due to Rossby wave energy propagation, as represented by the wave activity flux vectors in the latitudes between 45°N and 70°N over northern Eurasia. These emanate from the initial development region of the wave train over northeastern Europe close to Scandinavia and European Russia. The most prominent signature in the wave activity flux vector field is that it has stronger eastward and southeastward flux across northern Eurasia,

especially during phase 3 to phase 4 and phase 7 to phase 8. These are quite consistent with the downstream wave development over the eastern part of northern Eurasia.

Another interesting feature is that waves develop farther downstream into the North Pacific and North America. In phase 3, an isolated northern Eurasian wave packet ends off the east coast of Far East Asia. In the following phases, new anomalous troughs and ridges grow downstream and accompany eastward wave activity flux vectors along 40°N to 65°N over the North Pacific. The wave packet subsequently traverses the North Pacific and reaches North America in phase 4. A consecutive wave train, extending from northeastern Europe to the east coast of North America, is then created by phase 5. In phase 6, the wave train divides into two parts: the northern Eurasian part disperses into the northwest Pacific and the North American part progresses towards the northwestern Atlantic. In phase 7, the North American wave packet entirely dissipates, while the northern Eurasian wave packet remains and continues to propagate eastward. New anomalous troughs and ridges are continuously formed downstream over the North Pacific and North America from phase 8 to the next phase 1. Consequently, a consecutive wave train with an opposite sign to that in phase 5 is created in phase 1. However, the extent of the wave train associated with the 15-day oscillation is not completely circumglobal; rather, the wave train traverses about three-quarters of the mid- and high-latitude circle. The structure and propagation characteristics of this wave train are comparable to those observed by Kanaya (1986) and Jiang and Lau (2008), who reported summertime intraseasonal wave propagation in the mid- and high-latitudes. The nearly circumglobal wave propagation detected by Kanaya (1986) is similar to the wave train structure in phases 1 and 5 (Figure 9). The trans-Pacific wave train on the submonthly time scale defined by Jiang and Lau (2008) is also similar to the wave train extending from the North Pacific to North America that appears in phases 1, 4, 5, and 8 (Figure 9). It should also be noted that there is no organised wave propagation over the North Atlantic. The North American wave packet ends off the northwestern Atlantic and does not propagate farther downstream towards northwestern Europe. Successive wave propagation does not occur over the North Atlantic. Thus, the northern Eurasian wave train does not seem to be excited in the North Atlantic region.

Figure 10 displays large-scale circulation patterns governing the 45-day oscillation of precipitation. A geopotential height anomaly and the wave activity flux composites were constructed in a similar manner as in Figure 9, except that 25-day low-pass-filtered anomalies were used to capture lower-frequency intraseasonal waves relevant to the 45-day oscillation. The resulting circulation pattern is mainly characterised by a wave train that apparently emanates from the northeastern Atlantic and extends across northern Eurasia. The wave train has zonal wavenumbers of 3–4 over the northeastern Atlantic/northern Eurasian sector. Throughout the life cycle, the waves appear to have mixed standing and propagating characteristics. In phase 2, the wave train forms a clear tripole pattern with a ridge over the northeastern Atlantic, a trough over northeastern Europe, and a ridge over western-central Siberia. As part of this wave train, a trough–ridge couplet which consists of the northeastern European trough and the Siberian ridge prevails over the western part of northern Eurasia. Eastward–southeastward pointing wave activity flux vectors are aligned along the trough–ridge couplet. The trough–ridge couplet persists while moving slowly eastward and southeastward into Siberia from phase 2 to phase 3, although the northeastern Atlantic ridge rapidly decays. Similar quasi-stationary features are observed in a trough–ridge pattern with an opposite sign over the northeastern Europe–Siberian sector, between phases 6 and 8. The trough initially located over northeastern Europe travels eastward and southeastward into central Siberia from phase 2 to phase 8. The ridge also travels across almost the same path from phase 6 to phase 4 in the next cycle. The trough (ridge) weakens once in the downstream movement around phase 5 (phase 1), but remains and develops again from phase 6 (phase 2). This redevelopment may be due to Rossby wave energy propagation from upstream, as evidenced by the wave activity flux aligned along the wave train. Obviously, troughs and ridges, as parts of the wave train, correspond to the anomalous wet and dry zones, respectively, as seen in Figure 7. Throughout all these phases, the centre of the zonally elongated anomalous wet (dry) zone (Figure 7) is located to the east ahead of the trough (ridge). The eastward and southeastward phase propagation of the wet (dry) zone from European Russia into eastern Siberia (Figure 7) is accompanied by the movement of the trough (ridge) from Scandinavia into central-eastern Siberia from phase 2 to phase 8 (phase 6 to phase 4 in the next cycle). Thus, the wave train which spans the northeastern Atlantic–northern Eurasian sector produces the slow alternation of the wet and dry zones over northern Eurasia.

Overall, the well-organised wave activity associated with the 45-day oscillation is mostly over the northeastern Atlantic–northern Eurasian sector. There is little organised wave signal over the North Pacific, North America, and northwestern Atlantic. The waves do not exhibit successive downstream development towards the North Pacific–North American sector. The waves do not propagate deep into the North Pacific–North American sector. Amplification and decay of the waves occurs more locally in the northeastern Atlantic–northern Eurasian sector. These features are the largest differences from the wave train connected with the 15-day oscillation. The wave structure somewhat resembles that found by Iwao and Takahashi (2008). They detected the zonally oriented wave train across northern Eurasia associated with summertime Mongolian precipitation on intraseasonal time scales. However, the wave propagation path in our results appears to be rather northwest–southeast oriented compared to their results.

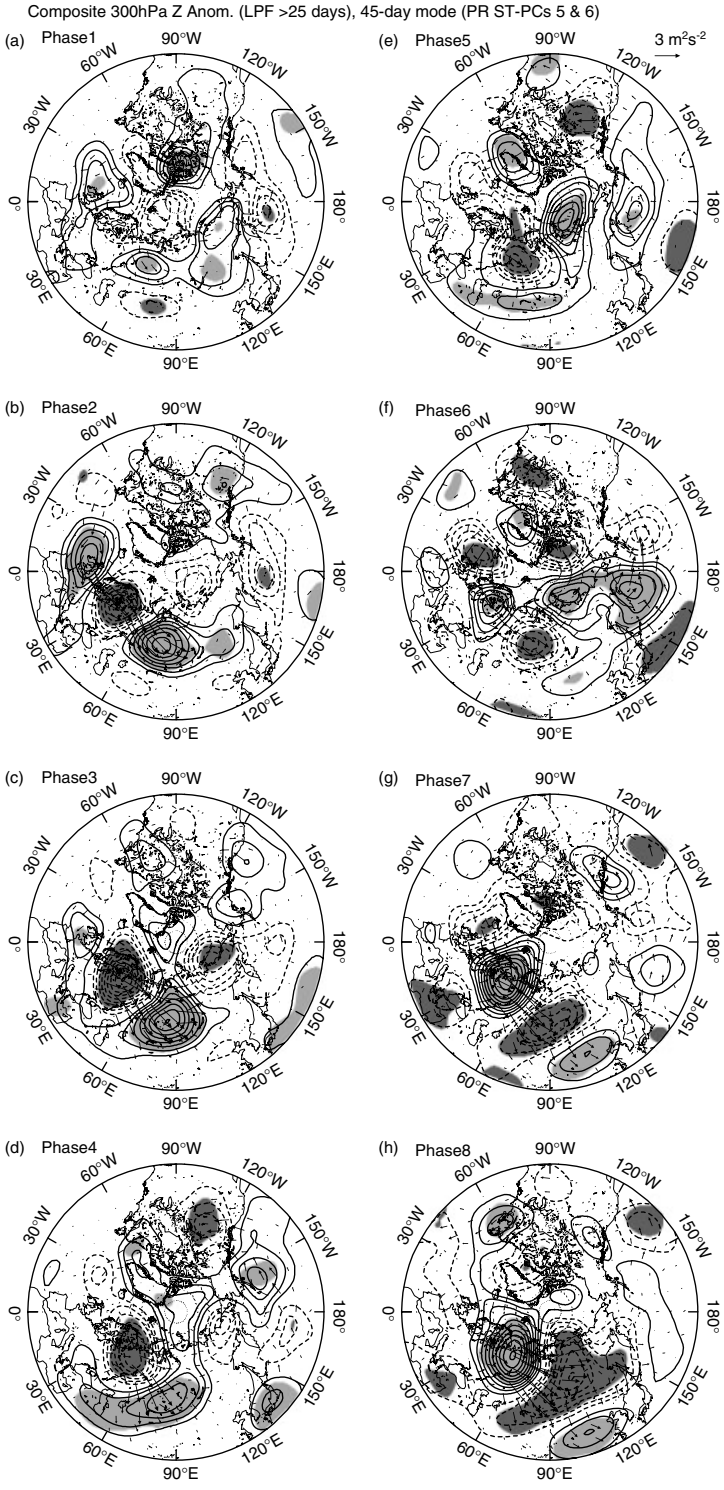

Figure 10. As in Figure 9 except for the 300-hPa geopotential height anomalies (25-day low-pass filtered) keyed to phase categories 1–8 of the 45-day oscillation. Contour interval is 20 m.

Finally, composite large-scale circulation patterns and corresponding wave activity flux vectors associated with the 9-day oscillation precipitation are presented in Figure 11. To represent the circulation patterns relevant to another submonthly scale mode, 6- to 12-day filtered 300-hPa geopotential height anomalies were used for compositing. The composite circulation pattern in each phase shows a wave train extending across northern Eurasia, consisting of a sequence of meridionally elongated anomalous troughs and ridges and dominated by zonal wavenumbers 6–7. Throughout the life cycle, the waves propagate eastward from Europe into Northeast Asia and the northwest Pacific. As the troughs and ridges travel eastward into Northeast Asia, they are amplified with their northeast to southwest elongation. The travelling troughs and ridges accompany the

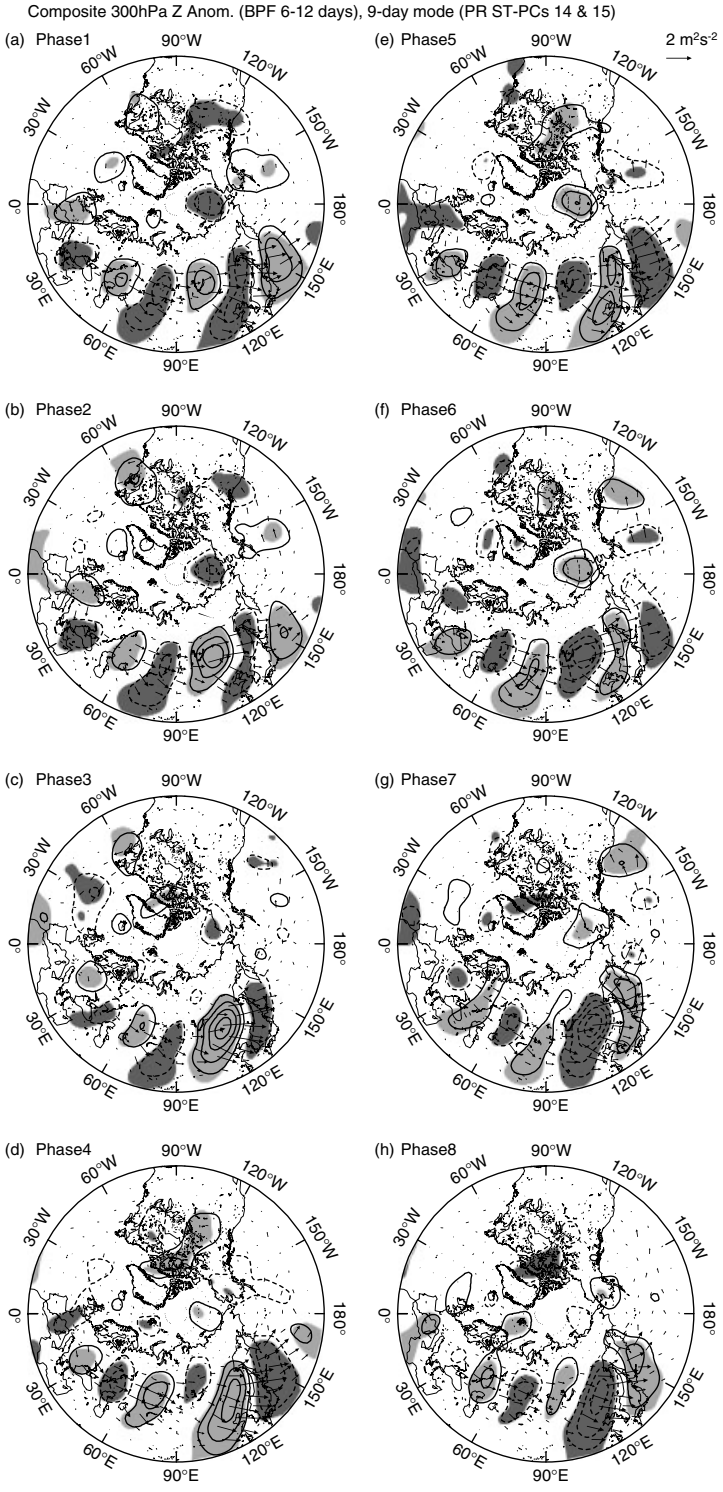

Figure 11. As in Figure 9 except for the 300-hPa geopotential height anomalies (6- to 12-day band-pass filtered) keyed to phase categories 1–8 of the 9-day oscillation.

eastward displacement of the anomalous wet and dry zones (Figure 8). The amplification of the troughs and ridges over Northeast Asia corresponds to the stronger precipitation fluctuations in the southern part of central-eastern Siberia (Figure 8). Interestingly, the amplified trough (ridge) over Northeast Asia, especially in phases 3 and 4 (phases 7–8), emanates enhanced wave activity fluxes towards the downstream (ridge) trough over the northwest Pacific. This suggests that the trough (ridge) over Northeast Asia is an important local wave energy source.

The overall wave train pattern displays similar structures in some respects to that associated with the 15-day mode (Figure 9) over northern Eurasia. The propagation properties of the 9-day wave are basically similar to those of the 15-day wave. However, the 9-day mode wave

train has a comparatively smaller spatial scale and its propagation path is located in the lower latitudes between approximately 35°N and 60°N. In addition, organised wave propagation is confined to northern Eurasia. The troughs and ridges which move into the northwest Pacific eventually dissipate over the northwest Pacific off the east coast of Northeast Asia and do not progress eastward into the North Pacific. Similarly, successive downstream development of the waves due to Rossby wave energy propagation does not occur in the North Pacific–North American sector.

7. Summary and discussion

This study analysed the intraseasonal variability of precipitation over northern Eurasia during the summers of 1979–2002. Dominant modes of intraseasonal oscillations of precipitation on different time scales were identified by applying MSSA to the gridded daily precipitation data. Three distinct oscillations were found in the MSSA spectral peaks centered at 15, 45, and 9 days. The spatiotemporal structures of these oscillations were revealed by constructing composite maps of the precipitation anomaly fields. The 15-day oscillation is the strongest oscillation and falls within the range of the so-called submonthly variability. The composite life cycle of the 15-day oscillation shows regular eastward phase propagation of precipitation anomalies, with a tripole structure across northern Eurasia. The 45-day oscillation lies within the range of low-frequency intraseasonal variability. The composite evolution of the 45-day oscillation exhibits a slowly varying signature with zonally elongated precipitation anomalies which are characterised by a broad east-west contrastive pattern across northern Eurasia. The 9-day oscillation falls within the higher frequency range of submonthly variability. While the spatiotemporal behaviours of the precipitation anomalies associated with this oscillation are similar to those of the 15-day oscillation, the spatial scale of this oscillation is somewhat smaller.

The composite evolution of 300-hPa geopotential height anomalies was also examined to highlight the large-scale circulation patterns connected to the life cycle of each oscillation of precipitation. The circulation anomalies linked to the 15-day oscillation exhibit an eastward propagating wave train extending from northeastern Europe into the North Pacific–North American sector. One of the interesting features of the wave-train behaviour is the nearly circumglobal propagation. The circulation patterns responsible for the 45-day oscillation are characterised by the wave train extending across the northeastern Atlantic–northern Eurasian sector. The wave train indicates the slowly eastward moving and quasi-stationary features. The well-organised wave train appears to be only over this sector and does not develop downstream towards the North Pacific–North American sector. The behaviour of the wave train pattern associated with the 9-day oscillation resembles that of the 15-day oscillation in the northern Eurasian sector. However, the wave train has a comparatively smaller spatial scale and wave propagation is confined to northern Eurasia.

The intraseasonal oscillations of precipitation found in this work are connected to the well-organised wave trains that extend from the Euro-Atlantic region to northern Eurasia. In general, the main precipitation producing system over northern Eurasia is an extratropical cyclone which accompanies precipitating fronts (Serreze *et al*., 2001; Serreze and Etringer, 2003; Fukutomi *et al*., 2007). The wave trains identified here could affect the strength of the cyclones and fronts and modulate subseasonal cyclogenic and frontal activities. The troughs (ridges) shown in the composite maps are coupled with anomalous wet (dry) zones. These zones must correspond to enhanced (reduced) precipitation associated with strengthened (weakened) frontal activities forced by the troughs (ridges) of the wave trains. Thus, the oscillation of precipitation on each intraseasonal time scale must be produced by the propagation of the corresponding wave train.

One can notice that the spectral characteristics in the MSSA-MEM results (Figure 4) and those in the FFT results for the selected domains (Figure 2) are not completely consistent with each other. The three distinct modes detected by the MSSA are not necessarily observed in the FFT results. For instance, peaks at nearly 15 and 45 days are not observed in the ensemble averaged spectra for the eastern domain (Figure 2(a)) and any significant peak at nearly 9 days is not found in those for the western domain (Figure 2(b)). One of the reasons for these inconsistencies could be due to a year-to-year variability of the spectral characteristics. By checking the spectra for individual years, we found out spectral peaks at nearly 15 and 45 days in several cases for the eastern domain (not shown). However, the ensemble averaging for the all cases could smooth the resulting spectra and diminish these peaks. The same reason might be applicable to the disappearance of a peak at 9 days in the western domain. The MSSA 9-day mode tends to have stronger signals in the southeastern Siberian domain and weaker signals in the western Siberian domain (Figure 8). This could also be a cause of the disappearance of a 9-day peak in the western domain. The 11-day signal in the FFT spectra for the eastern domain (Figure 2(a)) can be included in a category of the MSSA 15-day mode. The 15-day mode (ST-PCs 1-2) actually spans somewhat broader period range from about 11 days to 15 days (Figure 4). The similarities and differences between the MSSA and FFT results appear to be still open to discussion. We have tried to give possible explanations for those by considering the present results.

It is interesting to note the relationships between the intraseasonal oscillations and interannual variability of precipitation over northern Eurasia. Future study should examine subseasonal precipitation events associated with intraseasonal oscillations and interannual precipitation extremes. To ascertain the roles of the intraseasonal oscillations in producing interannual extremes,

classification of precipitation regimes is needed along with the associated circulation patterns on intraseasonal time scales. Cluster analysis would be a useful tool for this task. Investigation into the characteristics and occurrence frequency of intraseasonal precipitation regimes in extreme years should also be undertaken.

Acknowledgements

We appreciate the comments of anonymous reviewers, which helped to improve the article. Special thanks go to Akiyo Yatagai and Hisahiro Takashima for providing information on the data processing for APHRODITE's daily precipitation analysis (http://www.chikyu.ac.jp/precip/index.html).

References

Adam JC, Lettenmaier DP 2008. Application of new precipitation and reconstructed stream flow products to streamflow trend attribution in northern Eurasia. *Journal of Climate* **21**: 1807–1828.

Dettinger MD, Ghill M, Keppenne CL 1995. Interannual and interdecadal variability in United States surface-air temperatures, 1910–87. *Climatic Change* **31**: 35–66.

Fukutomi Y, Igarashi H, Masuda K, Yasunari T 2003. Interannual variability of summer water balance components in three major river Basins of northern Eurasia. *Journal of Hydrometeorology* **4**: 283–296.

Fukutomi Y, Masuda K, Yasunari T 2004. The role of storm track activity in the interannual seesaw of summer precipitation over northern Eurasia. *Journal of Geophysical Research* **109**: D02109, DOI: 10.1029/2003JD003912.

Fukutomi Y, Masuda K, Yasunari T 2007. Cyclone activity associated with the interannual seesaw oscillation of summer precipitation over northern Eurasia. *Global and Planetary Change* **56**: 387–398.

Fukutomi Y, Yasunari T 2005. Southerly surges on submonthly time scales over the eastern Indian Ocean during the Southern Hemisphere winter. *Monthly Weather Review* **133**: 1637–1654.

Iwao K, Takahashi M 2008. A precipitation seesaw mode between Northeast Asia and Siberia in summer caused by Rossby waves over the Eurasian continent. *Journal of Climate* **21**: 2401–2419.

Iwasaki H, Nii T 2006. The break in the Mongolian rainy season and its relation to the stationary Rossby wave along the Asian Jet. *Journal of Climate* **19**: 3394–3405.

Jiang N, Neelin D, Ghil M 1995. Quasi-quadrennial and quasi-biennial variability in the equatorial Pacific. *Climate Dynamics* **12**: 101–112.

Jiang X, Lau N-C 2008. Intraseasonal teleconnection between North America and western North Pacific monsoons with 20-day time scale. *Journal of Climate* **2**: 2664–2679.

Kanaya T 1986. An observational analysis of wave activities in different general circulation regimes for 1982 summer. *Journal of the Meteorological Society of Japan* **64**: 599–604.

Kaylor RE 1977. Filtering and decimation of digital time series. Tech. Note BN 850. Institute of Physical Science Technology, University of Maryland, College Park; 42.

Krishnamurthy V, Shukla J 2007. Intraseasonal and seasonally persisting patterns of Indian monsoon rainfall. *Journal of Climate* **20**: 3–20.

Krishnamurthy V, Shukla J 2008. Seasonal persistence and propagation of intraseasonal patterns over the Indian monsoon region. *Climate Dynamics* **30**: 353–369.

MacDonald GM, Kremenetski KV, Smith LC, Hidalgo HG 2007. Recent Eurasian river discharge to the Arctic Ocean in the context of long-term dendrohydrological records. *Journal of Geophysical Research* **112**: G04S50, DOI: 10.1029/2006JG000333.

McClelland JW, Holmes RM, Peterson BJ, Stielitz M 2004. Increasing river discharge in the Eurasian Arctic: consideration of dams, permafrost, and fires as potential agents of change. *Journal of Geophysical Research* **109**: D18102, DOI: 10.1029/2004JD004583.

Moron V 1997. Trend, decadal and interannual variability in annual rainfall of subequatorial and tropical North Africa. *International Journal of Climatology* **17**: 785–805.

Moron V, Vautard VR, Ghil M 1998. Trends, interdecadal and interannual oscillations in global sea-surface temperatures. *Climate Dynamics* **14**: 545–569.

Onogi K, Koide H, Sakamoto M, Kobayashi S, Tsutsui J, Hatsushika H, Matsumoto T, Yamazaki N, Kamahori H, Takahashi K, Kato K, Oyama R, Ose T, Kadokura S, Wada K. 2005. JRA-25: Japanese 25-year reanalysis–progress and status. *Quarterly Journal of the Royal Meteorological Society* **131**: 3259–3268.

Onogi K, Tsutsui J, Koide H, Sakamoto M, Kobayashi S, Hatsushika H, Matsumoto T, Yamazaki N, Kamahori H, Takahashi K, Kadokura S, Wada K, Kato K, Oyama R, Ose T, Mannouji N, Taira R. 2007. The JRA-25 analysis. *Journal of the Meteorological Society of Japan* **85**: 369–432.

Pavelsky TM, Smith LC 2006. Intercomparison of four global precipitation data sets and their correlation with increased Eurasian river discharge to the Arctic Ocean. *Journal of Geophysical Research* **111**: D21112, DOI: 10.1029/2006JD007230.

Peng S, Mysak LA 1993. A teleconnection study of interannual sea surface temperature fluctuations in the northern North Atlantic and precipitation and runoff over western Siberia. *Journal of Climate* **6**: 876–885.

Peterson BJ, Holmes RM, McClelland JW, Vorosmarty CJ, Lammers RB, Shiklomanov AI, Shiklomanov IA, Rahmstorf S 2002. Increasing river discharge into the Arctic Ocean. *Science* **298**: 2171–2173.

Plaut G, Vautard R 1994. Spells of low-frequency oscillations and weather regimes in the Northern Hemisphere. *Journal of Atmospheric Science* **51**: 210–236.

Qian B, Xu H, Corte-Real J 2000. Spatial-temporal structures of quasi-periodic oscillations in precipitation over Europe. *International Journal of Climatology* **20**: 1583–1598.

Rawlins MA, Willmott CJ, Shiklomanov A, Linder E, Frolking S, Lammers RB, Vorosmarty CJ 2006. Evaluation of trends in derived snowfall and rainfall across Eurasia and linkages with discharge to the Arctic Ocean. *Geophysical Research Letters* **33**: L07403, DOI: 10.1029/2006GL025231.

Semiletov IP, Savelieva NI, Weller GE, Pipko II, Pugach SP, Gukov AY, Vasilevskaya LN 2000. The dispersion of Siberian river flows into coastal waters: Meteorological, hydrological and hydrochemical aspects. In *The Freshwater Budget of the Arctic Ocean, NATO Science Series 2: Environmental Security 47*, Lewis EL, Jones EP, Lemke P, Prowse TD, Wadhams P (eds). Kluwer Academic Publishers: Dordrecht, The Netherlands; 323–366.

Serreze MC, Bromwich DH, Clark MP, Etringer AJ, Zhang T, Lammers R 2003. The large-scale hydro-climatology of the terrestrial Arctic drainage system. *Journal of Geophysical Research* **108**: ALT 1-1–ALT 1-28, DOI: 10.1029/2001JD000919.

Serreze MC, Etringer AJ 2003. Precipitation characteristics of the Eurasian Arctic drainage system. *International Journal of Climatology* **23**: 1267–1291.

Serreze MC, Lynch AH, Clark MP 2001. The Arctic frontal zone as seen in the NCEP–NCAR reanalysis. *Journal of Climate* **14**: 1550–1567.

Simonnet E, Plaut G 2001. Space–time analysis of geopotential height and SLP, intraseasonal oscillations, weather regimes, and local climates over the North Atlantic and Europe. *Climate Research* **17**: 325–342.

Takashima H, Yatagai A, Kawamoto H, Arakawa O, Kamiguchi K 2009. Hydrological balance over northern Eurasia from gauge-based high-resolution daily precipitation data. In *From Headwaters to the Ocean: Hydrological Change and Water Management*, Taniguchi M (ed.). Taylor & Francis: London; 37–42.

Takaya M, Nakamura H 1997. A formulation of a wave-activity flux for stationary Rossby waves on a zonally varying basic flow. *Geophysical Research Letters* **24**: 2985–2988.

Takaya M, Nakamura H 2001. A formulation of a phase-independent wave-activity flux for stationary and migratory quasigeostrophic eddies on a zonally varying basic flow. *Journal of Atmospheric Sciences* **58**: 608–627.

Wang XL, Cho H-R 1997. Spatial-temporal structures of trend and oscillatory variability of precipitation over northern Eurasia. *Journal of Climate* **10**: 2285–2298.

Wang XL, Corte-Real J, Zhang X 1996a. Low-frequency oscillations and associated wave motions over Eurasia. *Tellus* **48A**: 238–253.

Wang XL, Corte-Real J, Zhang X 1996b. Intraseasonal oscillations and associated spatial-temporal structures of precipitation over China. *Journal of Geophysical Research* **101**: 19035–19042.

Yatagai A, Arakawa O, Kamiguchi K, Kawamoto H, Nodzu M, Hamada A 2009. A 44-year daily gridded precipitation dataset for

Asia based on a dense network of rain gauges. *SOLA* **5**: 137–140, DOI: 10.2151/sola.2009-035.

Yatagai A, Xie P, Alpert P 2008. Development of a daily gridded precipitation data set for the Middle East. *Advances in Geosciences* **12**: 165–170.

Ye H, Cho H-R 2001. Spatial and temporal characteristics of intraseasonal oscillations of precipitation over the United States. *Theoretical and Applied Climatology* **68**: 51–66.

Yoon J-H, Chen T-C 2006. Maintenance of the boreal forest rainbelts during northern summer. *Journal of Climate* **19**: 1437–1449.

Zhang X, Corte-Real J, Wang XL 1997. Low-frequency oscillations in the Northern Hemisphere. *Theoretical and Applied Climatology* **57**: 125–133.

Zhang X, Sheng J, Shabbar A 1998. Modes of interannual and interdecadal variability of Pacific SST. *Journal of Climate* **11**: 2556–2569.

